A highly magnified candidate for a young galaxy seen when the Universe was ∼500 Myr old

Wei Zheng[1], Marc Postman[2], Adi Zitrin[3], John Moustakas[4,5], Xinwen Shu[6], Stephanie Jouvel[7,8], Ole Høst[7], Alberto Molino[9], Larry Bradley[2], Dan Coe[2], Leonidas A. Moustakas[10], Mauricio Carrasco[11], Holland Ford[1], Narciso Benítez[9], Tod R. Lauer[12], Stella Seitz[13], Rychard Bouwens[14], Anton Koekemoer[2], Elinor Medezinski[1], Matthias Bartelmann[3], Tom Broadhurst[15,16], Megan Donahue[17], Claudio Grillo[18], Leopoldo Infante[11], Saurabh W. Jha[19], Daniel D. Kelson[20], Ofer Lahav[7], Doron Lemze[1], Peter Melchior[21], Massimo Meneghetti[22], Julian Merten[10], Mario Nonino[23], Sara Ogaz[2], Piero Rosati[24], Keiichi Umetsu[25], Arjen van der Wel[26]

[1] *Department of Physics & Astronomy, Johns Hopkins University, Baltimore, MD 21218, USA*

[2] *Space Telescope Science Institute, Baltimore, MD 21218, USA*

[3] *Institut für Theoretische Astrophysik, Universität Heidelberg, 69120 Heidelberg, Germany*

[4] *Center for Astrophysics & Space Sciences, University of California, San Diego, La Jolla, CA 92093, USA*

[5] *Department of Physics & Astronomy, Siena College, Loudonville, NY 12211, USA*

[6] *Department of Astronomy, University of Science & Technology of China, Hefei, Anhui 230026, China*

[7] *Department of Physics & Astronomy, University College London, London WC1E 6BT, UK*

[8] *Institute de Ciencies de l'Espai, 08193 Bellaterra, Spain*

[9] *Instituto de Astrofísica de Andalucía, E-18008 Granada, Spain*

[10] *Jet Propulsion Laboratory, California Institute of Technology, Pasadena CA 91109, USA*

[11] *Departamento de Astronomía y Astrofísica, Pontificia Universidad Católica de Chile, Santiago 22, Chile*

[12] *National Optical Astronomical Observatory, Tucson, AZ 85726, USA*

[13] *Universitäts-Sternwarte München, D-81679 München, Germany*

[14] *Leiden Observatory, Leiden University, 2300 RA Leiden, The Netherlands*

[15]Department of Theoretical Physics, University of Basque Country, 48080 Bilbao, Spain

[16]Ikerbasque, Basque Foundation for Science, Spain

[17]Department of Physics & Astronomy, Michigan State University, East Lansing, MI 48824, USA

[18]Dark Cosmology Centre, Niels Bohr Institute, University of Copenhagen, 2100 Copenhagen, Denmark

[19]Department of Physics & Astronomy, Rutgers University, Piscataway, NJ 08854, USA

[20]The Observatories of the Carnegie Institution for Science, Pasadena, CA 91101, USA

[21]Department of Physics, The Ohio State University, Columbus, OH 43210, USA

[22]INAF-Osservatorio Astronomico di Bologna, I-40127 Bologna, Italy

[23]INAF-Osservatorio Astronomico di Trieste, 40131 Trieste, Italy

[24]European Southern Observatory, D-85748 Garching, Germany

[25]Academia Sinica, Institute of Astronomy & Astrophysics, Taipei 10617, Taiwan

[26]Max-Planck Institut für Astronomie, D-69117 Heidelberg, Germany

Re-ionization of the intergalactic medium occurs in the early Universe at redshift $z\sim$6-11, following the formation of the first generation of stars[1]. Those young galaxies (where the bulk of stars form) at the early cosmic age of $\lesssim$500 million years (Myr, $z \gtrsim 10$) remain largely unexplored as they are at or beyond the sensitivity limits of current large telescopes. Yet, understanding the properties of these galaxies is critical to identifying the source of the ionizing radiation in the early universe. Gravitational lensing by galaxy clusters enables the detection of high-redshift galaxies that are fainter than what otherwise could be found in the deepest images of the sky[2]. Here we report the discovery of an object found in the multi-band observations of the cluster MACS1149+2223 that has a high probability of being a gravitationally magnified galaxy from the early universe, at a redshift of z = 9.6 $\pm$ 0.2 (*i.e.*, 490$\pm$15 Myr or 3.6% of the age of the Universe). We estimate that its age is less than 200 Myr (at the 95% confidence level), implying a formation redshift of $z_f \lesssim 14$.

Galaxy clusters are the largest reservoirs of gravitationally bound dark matter (DM), whose huge mass bends light and forms "cosmic lenses." They can significantly magnify the brightness and sizes of galaxies far behind them, thereby revealing morphological details that are otherwise impossible to detect[3–8] and enabling spectroscopy to study the physical conditions in these intrinsically faint galaxies. Most galaxies at $z \sim 10$ are expected to be fainter than magnitude of ~ 29 (in the AB system, used hereafter)[9–11], below the imaging detection limits of the deepest fields observed by *Hubble Space Telescope* (*HST*), and largely beyond the spectroscopic capability of even the next generation of large telescopes. A gain in sensitivity through gravitational lensing is particularly valuable for the *Spitzer Space Telescope* infrared data because the telescope's low spatial resolution blends faint sources and hampers extremely deep observations.

By combining the *HST* and *Spitzer* data we are able to estimate the age of such distant objects based on the ratio of their rest-frame ultra-violet to optical fluxes. The age and distance estimates rely, in large part, on measuring the observed wavelengths and relative amplitudes of prominent Hydrogen absorption features in the spectra of faint galaxies. At $z > 7$, the Hydrogen Lyα break, at $\sim 0.12(1+z)$ μm, is redshifted out of the optical bands, and the Hydrogen Balmer break, at $\sim 0.38(1+z)$ μm, is redshifted into the *Spitzer*/IRAC (Infrared Array Camera) range.

We have discovered a gravitationally lensed source whose most likely redshift is $z \sim 9.6$. The source, hereafter called MACS1149-JD, is selected from a near-infrared detection image at significance of 22σ. MACS1149-JD has a unique flux distribution characterized by a) no detection at wavelengths shorter than 1.2 μm, b) firm detections in the two reddest *HST* bands and c) weak detections in two other *HST*/WFC3/IR (Wide-Field Camera 3/Infrared Channel) bands and in one *Spitzer*/IRAC channel (Fig. 1). The object's coordinates (J2000) are: RA=$11^h49^m33^s.584$ Dec=+$22^\circ 24' 45''.78$ (Fig. 2).

The Cluster Lensing And Supernova survey with Hubble (CLASH)[12] is a *HST* Multi-Cycle Treasury program that is acquiring images in 16 broad bands between $0.2 - 1.7$ μm for 25 clusters. MACS J1149.6+2223 is a massive cluster ($\sim 2.5 \times 10^{15}$ $M_\odot$ [solar masses]) at redshift $z = 0.544$, selected from a sample of X-ray luminous clusters[13]. The mass models for this cluster[14,15] suggest a relatively flat mass distribution profile and a large area of high magnification, making it one of the most powerful cosmic lenses known.

The spectral-energy distribution (SED) features of galaxies, most notably the Lyman break and the Balmer break, generate distinct colors between broad bands and enable us to derive their redshifts with reasonable accuracy. Our photometric redshift estimates are made with two different techniques: Le Phare (LPZ)[16] and Bayesian Photometric Redshifts (BPZ)[17]. LPZ photometric redshifts are based on a template fitting procedure with a maximum likelihood (χ^2) estimate. We use the template library of the COSMOS survey[18], including galaxy templates of three ellipticals, seven spirals[19] and 12 common templates[20], with starburst ages ranging from 30 Myr to 3 Gyr (billion years) to better reproduce the bluest galaxies. The LPZ solution from the marginalized posterior is $z = 9.60^{+0.20}_{-0.28}$ (at 68% confidence level), and the best-fit model is a starburst galaxy.

BPZ multiplies the likelihood by the prior probability of a galaxy with an apparent magnitude m_0 of having a redshift z and spectral type T. We run BPZ using a new library composed of 11 SED templates originally drawn from PEGASE[21] but recalibrated using the FIREWORKS photometry and spectroscopic redshifts[22] to optimize its performance. This galaxy library includes five templates for ellipticals, two for spirals, and four for starbursts. The most likely BPZ solution is a starburst galaxy at $z = 9.61^{+0.14}_{-0.13}$ (1σ).

Even though the CLASH data have more bands than other *HST* projects, MACS1149-JD is detected only in the four reddest *HST* bands. The high confidence of our high-redshift solution is enabled by the IRAC photometry at 3.6μm and 4.5μm. With *HST* data alone (*i.e.*, excluding *Spitzer* data) solutions with intermediate redshifts ($2 \lesssim z \lesssim 6$) can be found but they have low probability (Fig. 3). When *Spitzer* data are included, no viable solutions other than those at $z \sim 9.6$ are found, and the possibility for photometric redshifts $z < 8.5$ is rejected at 4σ confidence level ($< 3 \times 10^{-5}$).

Using confirmed multiply lensed images, strong-lensing (SL) models[14,23] allow us to derive the mass distribution of DM in the cluster, which leads to an amplification map for background sources. With 23 multiply lensed images of seven sources, some of which are large enough to comprise distinctive knots used as additional constraints, we derive the best-fit model in which the critical curve (defining regions of high magnification) for $z \sim 10$ extends to the vicinity of MACS1149-JD, resulting in a magnification of $\mu = 14.5^{+4.2}_{-1.0}$. The results are in rough agreement with a second, independent model[24], which yields a best-fit magnification with large error bars, $26.6^{+20.8}_{-7.7}$.

Because our data cover a broad spectral range in the object's rest frame, we are able to estimate some key properties for the source using the Bayesian SED-fitting code `iSEDfit`[25] coupled to state-of-the-art models of synthetic stellar populations [26] and based on the Chabrier[27] initial mass function from (IMF) $0.1-100$ $M_{\odot}$. We consider a wide range of parameterized star formation histories and stellar metallicities and assume no dust attenuation in our fiducial modeling (but see the *Supplementary Information*), as previous studies[28,29] found no evidence for dust in galaxies at the highest redshifts.

Fig. 4 presents the results of our population synthesis modeling adopting $z = 9.6$ as the source redshift. Based on the median of the posterior probability distributions, our analysis suggests a stellar mass of $\sim 1.5 \times 10^{8}$ $(\mu/15)^{-1}$ $M_{\odot}$ and a star-formation rate (SFR) of ~ 1.2 $(\mu/15)^{-1}$ $M_{\odot}$ year^{-1}. Note that these values would be up to a factor of eight higher if dust attenuation is not negligible (see the *Supplementary Information*). Given the uncertainties in the IRAC photometry, we are unable to measure the age of the galaxy precisely; however, we can constrain its SFR-weighted age, or the age at which most of the stars formed, to $\langle t \rangle_{\rm SFR} < 200$ Myr (95% confidence level), suggesting a likely formation redshift $z_f < 14.2$. Given that the source is brighter at 4.5μm than at 3.6μm, the presence of a Balmer break is likely, suggesting that MACS1149-JD may not be extremely young. This age implies a formation redshift of no earlier than $z_f \approx 11.3$, and is generally consistent with the estimated ages ($\gtrsim 100$ Myr) of galaxies at slightly lower redshifts, $z \sim 7-8$.[30]

Based on a single discovery of MACS1149-JD over 12 clusters and our corresponding lensing models, we estimate that the SFR density at $z = 9{-}10$ is $(1.8^{+4.3}_{-1.1}) \times 10^{-3}$ $M_\odot$ Mpc^{-3} (per cubic megaparsec) year^{-1}, lower than the extrapolation from lower redshifts[9], but higher than the limit derived from the HUDF (Hubble Ultra Deep Field)[9]. Statistically, our estimate is consistent with both values, and more data are needed to reduce the uncertainties. Our current observations, coupled with knowledge of the galaxy luminosity function[1], suggest that faint galaxies at $z \sim 10$ may well be the dominant source for the early re-ionization of the intergalactic medium.

1. Robertson, B. E., Ellis, R. S., Dunlop, J. S., McLure, R. J. & Stark, D. P. Early star-forming galaxies and the reionization of the Universe, *Nature*, **468**, 49-55 (2010).

2. Kneib, J.-P. & Natarajan, P. Cluster lenses, *Astron. Astrophys. Rev.*, **19**, 47-146 (2011).

3. Kneib, J.-P., Ellis, R. S., Santos, M. R. & Richard, J., A probable $z \sim 7$ galaxy strongly lensed by the rich cluster A2218: exploring the dark ages, *Astrophys. J.*, **607**, 697-703 (2004).

4. Bradley, L. D., et al. Discovery of a very bright strongly lensed galaxy candidate at $z \sim 7.6$, *Astrophys. J.*, **678**, 647-654 (2008).

5. Zheng, W., et al. Bright strongly lensed galaxies at redshift $z \sim 6-7$ behind the clusters Abell 1703 and CL0024+16, *Astrophys. J.*, **697**, 1907-1917 (2009).

6. Richard, J., et al. Discovery of a possibly old galaxy at $z = 6.027$, multiply imaged by the massive cluster Abell 383, *Mon. Not. R. Astron. Soc.*, **414**, L31-35 (2011).

7. Bradley, L. D., et al. Through the looking glass: bright, highly magnified galaxy candidates at $z \sim 7$ behind A1703, *Astrophys. J.*, **747**, 3 (2012).

8. Zitrin, A., et al. CLASH: Discovery of a bright $z \simeq 6.2$ dwarf galaxy quadruply lensed by MACS J0329.6-0211, *Astrophys. J.*, **747**, L9 (2012).

9. Bouwens, R. J., et al. A candidate redshift $z \approx 10$ galaxy and rapid changes in that population at an age of 500 Myr, *Nature*, **469**, 504-507 (2011).

10. Oesch, P. A., et al. Expanded search for $z \sim 10$ galaxies from HUDF09, ERS, and CANDELS data: evidence for accelerated evolution at $z > 8$? *Astrophys. J.*, **745**, 110 (2012).

11. Zackrisson, E., et al. Detecting gravitationally lensed population III galaxies with HST and JWST, astro-ph/1204.0517 (2012).

12. Postman, M., et al. Cluster lensing and supernova survey with Hubble (CLASH): an overview, *Astrophys. J. Suppl.*, **199**, 25 (2012).

13. Ebeling, H., Edge A. C., & Henry J. P. MACS: A quest for the most massive galaxy clusters in the universe, *Astrophys. J.*, **553**, 668-676 (2001).

14. Zitrin, A., & Broadhurst, T. Discovery of the largest known lensed images formed by a critically convergent lensing cluster, *Astrophys. J.*, **703**, L132-136 (2009).

15. Smith, G. P., et al. Hubble space telescope observations of a spectacular new strong-lensing galaxy cluster: MACS J1149.5+2223 at z = 0.544, *Astrophys. J.*, **707**, L163-168 (2009).

16. Ilbert, O., et al. Accurate photometric redshifts for the CFHT legacy survey calibrated using the VIMOS VLT deep survey, *A&Ap*, **457**, 841-856 (2006).

17. Benítez, N. Bayesian photometric redshift estimation, *Astrophys. J.*, **536**, 571-583 (2000).

18. Koekemoer, A. M., et al. The COSMOS survey: Hubble space telescope advanced camera for surveys observations and data processing, *Astrophys. J. Suppl.*, **172**, 196-202 (2007).

19. Polletta, M. et al. Spectral energy distributions of hard X-Ray selected active galactic nuclei in the XMM-Newton medium deep survey, *Astrophys. J.*, **663**, 81-102 (2007).

20. Bruzual, G., & Charlot, S. Stellar population synthesis at the resolution of 2003, *Mon. Not. R. Astron. Soc.*, **344**, 1000-1028 (2003).

21. Fioc, M., & Rocca-Volmerange, B. PEGASE: a UV to NIR spectral evolution model of galaxies. application to the calibration of bright galaxy counts, *A&Ap*, **326**, 950-962 (1997).

22. Wuyts, S., et al., FIREWORKS U_{38}-to-24μm photometry of the GOODS Chandra deep field-south: multiwavelength catalog and total infrared properties of distant K_s-selected galaxies, *Astrophys. J. Suppl.*, **682**, 985-1003 (2008).

23. Zitrin, A., Broadhurst, T., Barkana, R., Rephaeli, Y., & Benítez, N. Strong-lensing analysis of a complete sample of 12 MACS clusters at $z > 0.5$: mass models and Einstein radii, *Mon. Not. R. Astron. Soc.*, **410**, 1939-1956 (2011).

24. Jullo, E., et al. A Bayesian approach to strong lensing modelling of galaxy clusters, *New J. Phys.*, **9**, 447 (2007).

25. Moustakas, J., et al. Evolution of the stellar mass-metallicity relation since $z = 0.75$, *Astrophys. J.*, submitted, arXiv 1112.3300 (2011).

26. Conroy, C., & Gunn, J. E. The propagation of uncertainties in stellar population synthesis modeling. III. model calibration, comparison, and evaluation, *Astrophys. J.*, **712**, 833-857 (2010).

27. Chabrier, G. Galactic stellar and substellar initial mass function, *Pub. Astr. Soc. Pac.*, **115**, 763-795 (2003).

28. Labbé, I., et al. Ultradeep infrared array camera observations of sub-L* $z \sim 7$ and $z \sim 8$ galaxies in the Hubble ultra deep field: the contribution of low-luminosity galaxies to the stellar mass density and reionization, *Astrophys. J.*, **708**, L26-31 (2010).

29. Bouwens, R. J., et al. Very blue UV-continuum slope β of low luminosity $z \sim 7$ galaxies from WFC3/IR: evidence for extremely low metallicities? *Astrophys. J.*, **708**, L69-73 (2010).

30. Labbé, I., et al. Star formation rates and stellar masses of $z = 7 - 8$ galaxies from IRAC observations of the WFC3/IR early release science and the HUDF fields, *Astrophys. J.*, **716**, L103-108 (2010).

Acknowledgments The CLASH program (GO-12065) is based on observations made with the NASA/ESA *Hubble Space Telescope*. The Space Telescope Science Institute is operated by the Association of Universities for Research in Astronomy, Inc. under NASA contract NAS 5-26555. This work is also based in part on archival data obtained with the *Spitzer Space Telescope*, which is operated by the Jet Propulsion Laboratory, California Institute of Technology under a contract with NASA.

Author Contributions W.Z. made the initial identification and wrote a draft. R.B., D.C., H.F. and L.B. verified the target selection. M.P and H.F performed comparisons with intermediate-redshift and nearby objects and edited the final version. W.Z., A.K., L.B., D.C., S.O. and E.M. processed the *HST* data. X.S., W.Z. and L.A.M. performed the IRAC photometry. S.J., A.M., D.C., O.H. and N.B. made the redshift estimates. M.P., T.R.L. and L.B. performed the image deconvolution. J.M. carried out the SED fitting. A.Z., M.C. and T.B. constructed the lensing models. L.A.M. and D.C. estimated the SFR density at $z \sim 10$. The above authors also contributed the text and figures that describe their analyses. P.R., L.I., P.M., M.N., R.B. and L.A.M. contributed to the observing programs. M.B., M.D., C.G., S.W.J., D.D.K., O.L., D.L., P.M., K.U. and A.W. helped with the manuscript.

Correspondence Correspondence and requests for materials should be addressed to W.Z. (email: zheng@pha.jhu.edu).

Figure 1 – Multi-band images of the $z = 9.6$ galaxy candidate MACS1149-JD. The optical image is the sum of all ACS (Advanced Camera for Surveys) data. The source, located at the center of each image as marked by green circles, is firmly detected in the F140W (central wavelength 1.39 μm) and F160W (1.53 μm) bands and weakly detected in the F110W (1.15 μm) , F125W (1.25 μm) and 4.5μm bands. The F105W band (1.05 μm) extends to ~ 1.2 μm, and no detection in that band confirms no source flux below that wavelength. Each of these images is 10" on one side. North is up and east to the left. On the left side, an enlarged view of the F140W image shows its elongation, which is extended along a position angle of ~ 47 degrees. A yellow line marks the direction of shear predicted by the lensing model, and a red circle marks the aperture used for the source photometry (10 pixels in diameter).

Figure 2 – Composite color image of MACS J1149.6+2223 made from multi-band data. North is up and east to the left. The field of view is 2.2 arcmin on each side. The *z* = 9.6 critical curve for the best-fit lensing model is overplotted in white, and that for *z* = 3 is shown in blue. Green letters A-G mark the multiple images of seven sources that were used in the strong-lensing model. Yellow letters H and I mark the two systems that were not used in the final fitting. The location of MACS1149-JD is marked with a red circle, at RA=$11^h49^d33\overset{s}{.}584$ Dec=+$22^\circ24'45''.78$ (J2000).

Figure 3 – Probability distributions of photometric redshift estimation. All curves are normalized to their peak probability. Solid black curve: LPZ, using all the *HST* and *Spitzer* data; Solid red curve: BPZ with and without priors, using all data. Only the high-redshift solutions are confirmed with high confidence ($>$4σ). Dashed black curve: LPZ, using the *HST* data only. Dotted green curve: BPZ without priors, using the *HST* data only. In these two cases, intermediate-redshift solutions are present at low probability ($<$1%). Dotted magenta curve: BPZ with priors, using the *HST* data only. Only in such cases do intermediate-redshift solutions become significant.

Figure 4 – Stellar population synthesis modeling results for MACS1149-JD. The filled blue points mark bands in which the object is detected, while the open green triangles indicate 1σ upper limits. The errors in the F140W and F160W bands are small ($<$0.1 magnitude) and hence not visible. The black spectrum is the best-fit model, and the open red squares show the photometry of this model convolved with the WFC3, ACS, and IRAC filter response functions. The light blue shading shows the range of 100 additional models drawn from the posterior probability distribution that are also statistically acceptable fits to the data.

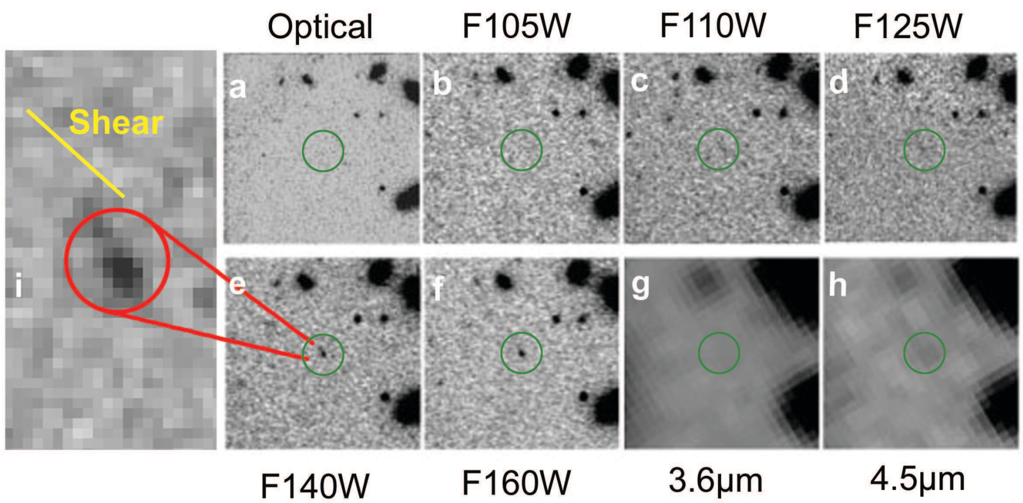
Optical
F105W
F110W
F125W
Shear
a
b
c
d
i
e
f
g
h
F140W
F160W
3.6μm
4.5μm

Figure 1

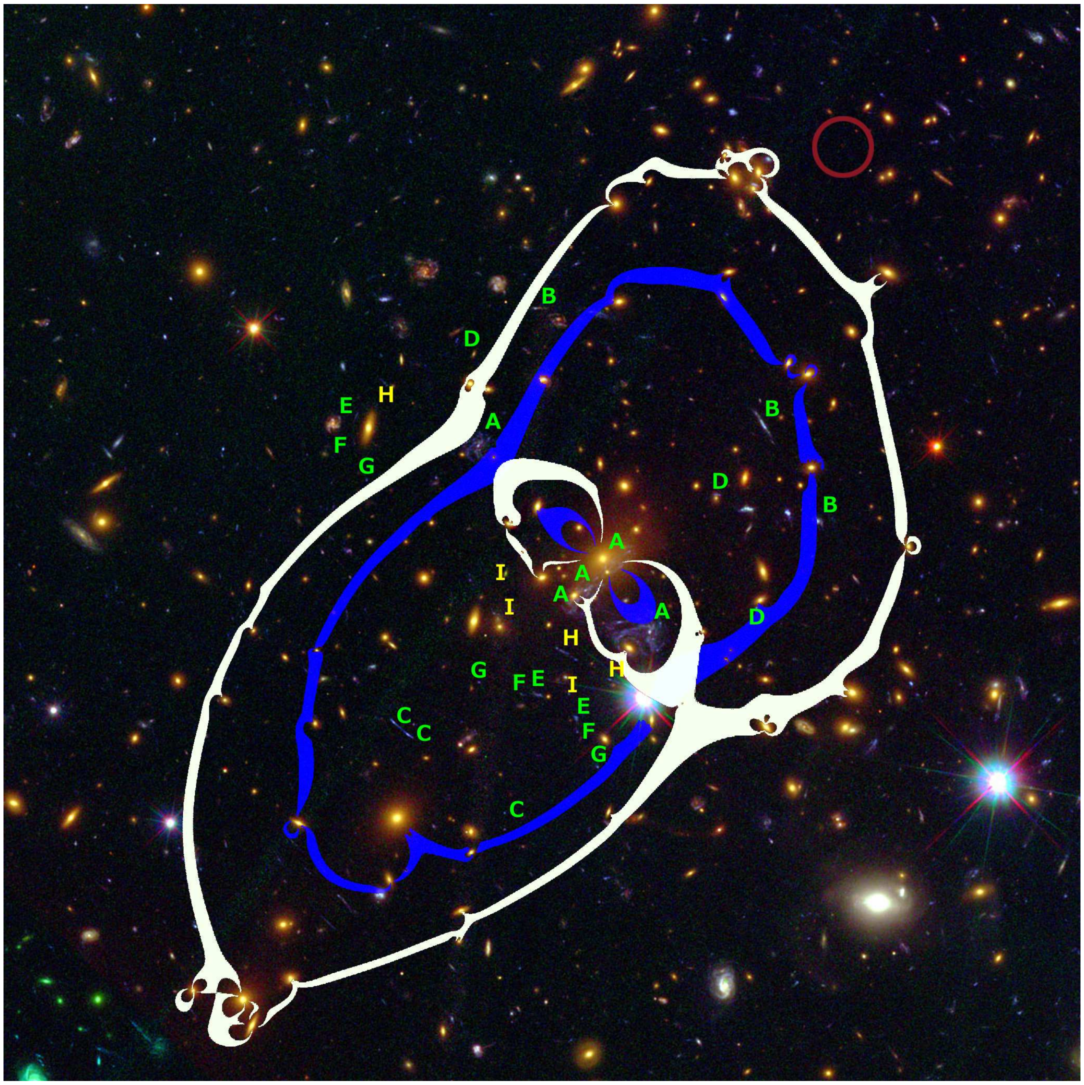

Figure 2

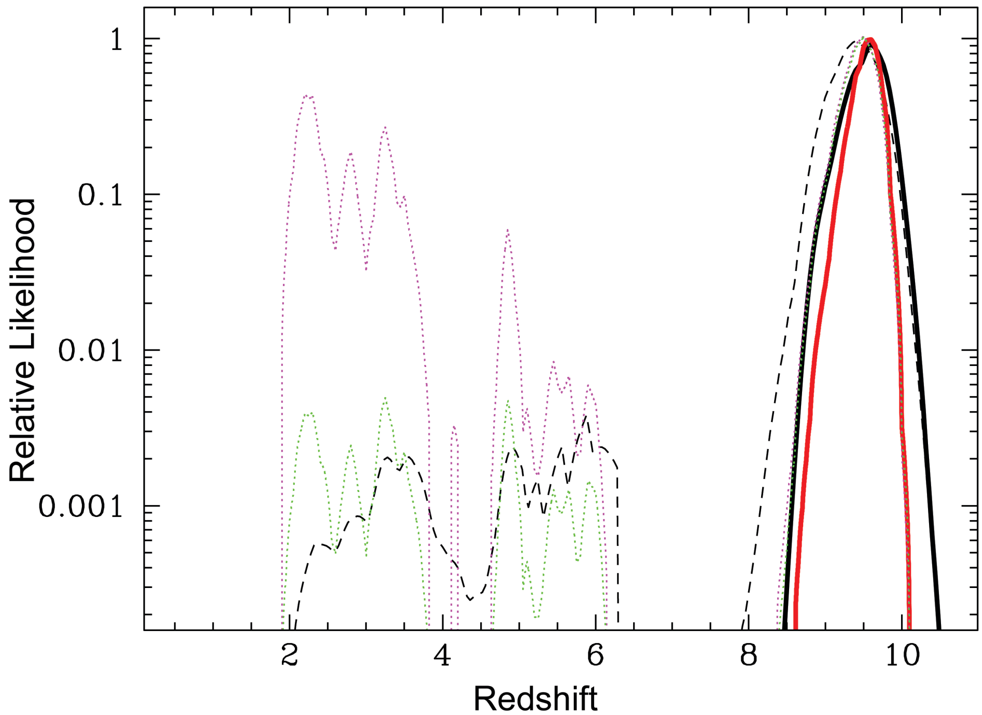

Figure 3

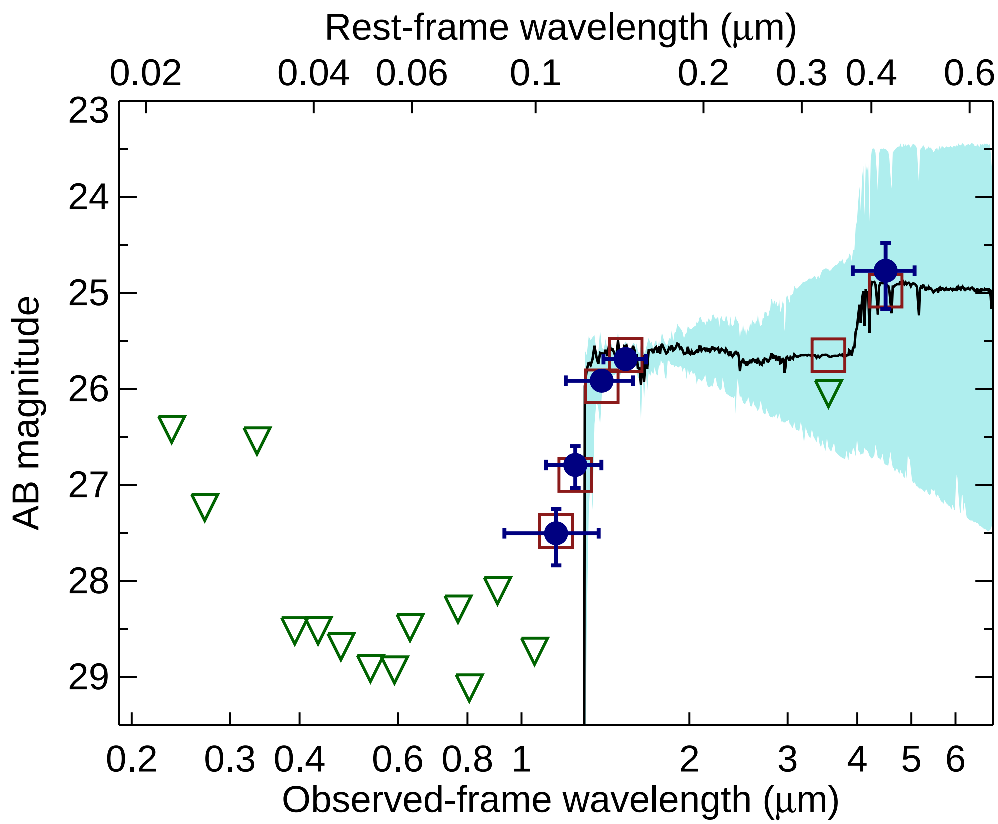
Rest-frame wavelength (μm)
0.02
0.04
0.06
0.1
0.2
0.3
0.4
0.6
23
24
25
26
27
28
29
AB magnitude
0.2
0.3
0.4
0.6
0.8
1
2
3
4
5
6
Observed-frame wavelength (μm)

Figure 4

Supplementary information

1. General outline

MACS1149-JD is found in a search of high-redshift galaxies in the observations of 12 CLASH clusters. Its characteristics are described here in further detail, along with our analysis methods. In §2 we describe the *HST* data processing, aperture photometry and target selection; in §3 the IRAC photometry is described; in §4 we test the intermediate-redshift probability of the source, using only part of the data; in §5 we discuss the lensing model and compare with another independent model; in §6 we describe the *HST* image deconvolution; in §7 we show our SED fitting method; in §8 we estimate the global SFR density based on this discovery; in §9 we demonstrate why the source is not a solar-system or Galactic interloper; in §10 we discuss the effect of photometric scattering of intermediate-redshift objects; and in §11 we summarize our tests.

We adopt the cosmological parameters $h = 0.7$, $\Omega_M = 0.3$, and $\Omega_\Lambda = 0.7$.

2. *HST* photometry and target selection

The CLASH observations of MACS J1149.6+2223 were carried out between December 2010 and March 2011. Previous archival *HST* images in the F555W and F814W bands were also used in our analyses. The data were processed in two independent pipelines: `APLUS`, an enhanced version of `APSIS`[31] that is now capable of merging and aligning WFC3 images, and `Multidrizzle`[32,33]. They were combined, aligned and re-sampled with a common pixel scale of 0″.065. A Subaru image, centered on the cluster and covering a 28×28 arcminute field, was used as the astrometric reference. Detection images were produced from the combination of ACS/WFC (Wide-Field Camera) and WFC3/IR images. We used the WFC3/IR detection image and ran `SExtractor`[34] in dual mode in every filter band.

Photometry was carried out with circular apertures whose diameter is between 2 and 20 pixels. At larger apertures, the source flux in each band increases and gradually approached an asymptotic value, and the spectral break became less prominent at larger apertures as more noise was added to each band. At each aperture size we estimated the photometric redshift, and the most precise photometric redshift was from the photometry made with an aperture of diameter 10 pixels ($0''.65$, see Figure 1). To verify the precision, we compared the source counts derived from our two independent pipelines and found that they agree well within the allowance of propagated errors. In the F140W and F160W bands, the count difference was $< 3\%$. The source magnitudes in these two bands were approximately 0.3 magnitude fainter than the values measured at an aperture of 20 pixels. We therefore corrected the source magnitude in each *HST* band by -0.3 magnitude (Table S1).

The $z \sim 10$ candidates were selected with the following criteria: (1) The difference in magnitude F110W$-$F140W > 1.3; (2) F140W$-$F160W < 0.5; and (3) No detection in the F105W band ($< 2\sigma$) and no detection in the optical detection image ($< 1\sigma$). MACS1149-JD is the only object in our database of 12 CLASH clusters observed to date that meets these criteria.

3. IRAC photometry

We retrieved archival *Spitzer*/IRAC images of MACS J1149.6+2223 observed in July 2010 and February 2011, under Program ID 60034 (PI: Egami), in the form of BCD (Basic Calibrated Data) and PBCD (Post BCD). The BCD data were processed with tasks *Overlap* and *Mosaic* in the `MOPEX` package to produce the final mosaic images with a pixel scale of $0''.6$. Individual PBCD images serve as the mosaics for each of the two epochs. The exposure times were 33.6 ksec in total and 16.8 ksec on target for both channels at 3.6 and 4.5 μm.

As the first step, two mosaic images taken at different epochs were used. In both epochs, the cluster was centered in the Channel 1 (3.6 μm) and 2 (4.5 μm) mosaics, and a visual inspection of the independent mosaics at 4.5 μm showed a clear detection at modest significance in both epochs. As the epochs were separated by six months, we ruled out the possibility of a spurious detection or a moving object (additional constraints in §8).

The candidate was not visually detected at 3.6μm in either epoch, or in the total stack, with a 1σ upper limit of magnitude 26.1. The sensitivity of the 3.6μm mosaic images was estimated by measuring the standard deviation of flux values in $2''.4$-diameter apertures randomly placed on empty background regions. The IRAC photometry at 4.5μm was carried out in several ways. We ran `GALFIT`[35] to fit the brightness profile of MACS1149-JD and neighboring sources simultaneously. A point-spread-function (PSF) image was made from the 4.5μm mosaic image by stacking four bright (magnitude ~ 18.5) and isolated stars. For bright neighboring foreground galaxies that could not be satisfactorily fitted with a pure PSF model, we assumed a generalized Sérsic profile and use the higher-resolution *HST*/WFC3 H-band image as a reference for the initial `GALFIT` input parameters.

Because of the importance of photometry in the 4.5μm band, we performed extensive tests to calibrate it. We constructed simulated point sources convolved with the IRAC PSF profile and normalized to magnitudes of 24.0, 24.5 and 25.0, respectively. We placed these simulated sources in the vicinity of MACS1149-JD, and ran `GALFIT` with different fitting windows (Figure S1) until the expected magnitude of each simulated source was recovered. We proceeded to fit the flux of MACS1149-JD without simulated sources, using the fitting window and background level on the image that recovered the brightness of the simulated sources most accurately. We repeated these tests at five different positions for the simulated sources of three different magnitudes to verify the measurements of the source magnitude. To account for the uncertainties in estimating the background at different positions around MACS1149-JD, we chose their mean value of 24.8 ± 0.3 as the source magnitude in the 4.5μm band.

We then used the above GALFIT results to subtract out the neighboring sources (but not MACS1149-JD itself), and performed aperture photometry using $2''.4$ diameter apertures. The local background was determined from an annulus of radius between 4 and 10 pixels. We found the source magnitude 26.0 ± 0.3, subject to a correction of -0.7 magnitude for the missing flux outside the aperture[36]. This magnitude derived from a small aperture was fainter by approximately 0.5 magnitude than that from GALFIT fitting. Note that the median of the pixel values in the sky annulus was used for the background estimation. We verified that the measured source flux could increase by $\sim 0.1 - 0.2$ magnitude if a smaller annulus for the sky was used (*e.g.* an outer radius of 8 pixels) to avoid the possible contamination from a few brighter pixels. While the measurement supported the GALFIT results that the source is detected, we did not use this value in Table S1 because of its larger uncertainty.

4. Intermediate-redshift probability

While our most probable and robust photometric redshift estimations yielded the high-redshift solution (Figure 3), we further studied alternative solutions not using the IRAC data in the fitting. Intermediate-redshift solutions were found at low probability when we ran LPZ and BPZ with only the four WFC3/IR bands where the source is detected. This is a conservative test as adding data in non-detection bands does reduce the likelihood for intermediate redshifts. These intermediate-redshift solutions all had considerably higher χ^2 values than the best fit solution at $z = 9.6$. For each model used, we calculated the χ^2 value from the estimations. LPZ yielded a best-fit model for a starburst galaxy at $z = 9.63 \pm 0.25$ with a low $\chi^2 = 5.1$ and degree of freedom (d.o.f) 16. Figure S2 shows the χ^2 values as a function of redshifts and the types of galaxy templates as the LPZ output. When the data in all 19 bands were included, only high-redshift solutions were found (panel a). When only the *HST* data where the source is detected (d.o.f = 1) was fitted, the χ^2 values for intermediate redshifts were unacceptably high (panel b).

Our photometric redshift estimations also included models with nebular emission, and the results were not affected by it. This is because the goodness-of-fit was heavily weighted by the position of the Lyα break in the WFC3/IR bands.

5. Lensing model

The basic assumption in our SL modeling approach is that light traces mass, so that the photometry of red sequence cluster members constituted the starting point of modeling. The mass model for each red sequence member was based on a surface-density power law, scaled by the galaxy's luminosity. The superposition of these power laws represented the lumpy, galaxy-scale mass component. This component was then smoothed by fitting a low-order polynomial to it, using two-dimensional (2D) spline interpolation, resulting in a smooth DM component. In total there were six fundamental free parameters[23]: the galaxy power law and the smoothing (polynomial) degree were the first two free parameters. The two mass components were then added with a relative galaxy-to-DM weight, which was the third free parameter. To the resulting deflection field, we added an external shear describing the overall ellipticity. The direction of the external shear and its magnitude were two additional free parameters. The overall scaling of the mass model was the last free fundamental parameter.

For galaxy distances, we used existing spectroscopic redshifts[15] and the accurate photometric redshifts derived via the CLASH multiband imaging. We generated preliminary six-parameter mass models using the multiple images and candidates presented in previous work[14,15] and also identified two new candidate systems (although these were not used for the minimization). The minimization for the final best-fit model was then implemented via a Monte Carlo Markov Chain (MC) with the Metropolis-Hastings algorithm[37] whose results we use here. The chain included six additional free parameters: the relative weight of the bright central galaxy and five other bright galaxies in the field, which allowed for a more accurate determination of the very inner mass profile. In addition, we allowed the redshift of the four systems with photometric redshifts to vary and be optimized by the model, introducing four additional free parameters.

The MC chain therefore minimized 16 free parameters, and included (after burn-in) a total of 20,000 steps with a typical $\sim 20\%$ acceptance rate. As constraints for the minimization, we used 23 secure multiple images of seven sources, whereas for system 1 as defined by Zitrin & Broadhurst[14], we used several distinctive knots across these large images as additional constraints. In total, 36 image+knot positions were used as constraints. Estimating the goodness-of-fit of the best-fit model from this chain (where throughout we adopted a $\sigma = 1''.4$ as the positional error in the χ^2 term), the χ^2, d.o.f and root-mean-square (rms) were 2.06, 30 and $1''.92$, respectively. This model yielded a magnification of $14.5^{+4.2}_{-1.0}$ for MACS1149-JD, while the median magnification from the MC chain was slightly higher: $15.5^{+3.3}_{-1.9}$.

In addition, we also generated a `Lenstool` mass model[24,38] to compare with our findings. The mass distribution and profile of the main halo were obtained by fitting the multiple-image information to a Navarro-Frenk-White profile[39]. We included the contribution of the brightest cluster galaxy and the 187 brightest member galaxies, each modeled by a truncated pseudo-isothermal elliptic mass distribution[40]. As constraints for the minimization, we used 21 secure multiple images of seven sources, adopting $\sigma = 1''.$ as the positional error. The goodness-of-fit for the best-fit model (out of a sample of 10,000 generated models) was $\chi^2 = 2.19$ (d.o.f 9), with an image-position rms error of $1''.71$ in the image plane. This complementary model therefore constitutes another independent measure, based on the adopted profile form that is different than our light-traces-mass assumption. With this best-fit model we found a magnification of $26.6^{+20.8}_{-7.7}$ for MACS1149-JD.

The magnification and shear of the two models agreed within the statistical errors. However, the value of the magnification factor close to the critical curves is a quantity that is sensitive to the model details, and one needs to also examine possible systematics. The comparison of the two modeling methods allowed us to estimate a systematic uncertainty of order of $\Delta\mu \sim 5$. Secondly, we checked the effect of the weight (or, the mass-to-light ratio) of the bright group of galaxies a few arcseconds south-east of the $z \simeq 9.6$ candidate image, since this could have a strong effect on the resulting magnification, and since these were fixed in both models. Correspondingly, we found that a reasonable 20% variation in the weights of these galaxies entail a magnification change of $\Delta\mu \sim 5$. To further examine possible systematics in the two methods, we generated two independent models using `Lenstool` (the first includes one central DM component, while the other which we incorporated here, models the cluster as two DM clumps), and several independent models using the method of Zitrin et al.[23], each with a different combination of free parameters (*i.e.*, different galaxies freely weighted, or photometric redshift optimizations). By doing so, we had a set of models to compare to the best fitting model used above, and assess the systematics these changes entail. We noted that some of these resulting models had critical curves (where the magnification diverges) that pass through the image or further outwards of its location, so that in principle, the upper systematic limit on the best-fit model magnification, was poorly constrained. Both of these models had in general a lower reduced χ^2 than the complementary chain models, and in particular, yielded better reproduction of images, as gauged by visual inspection. These were therefore chosen as the best-fit models used above and whose values we adopt throughout. We concluded that systematic uncertainties were of the same order as the statistical uncertainties, albeit with poorly constrained upper limits.

Our best-fit lens model predicted that MACS1149-JD lies outside the caustics for $z \sim 10$ in the source plane, so that it is likely not multiply lensed, but it was still predicted to be significantly magnified by gravitational lensing from the cluster. To examine the possibility of multiple images for MACS1149-JD, we chose a complementary MC chain model with somewhat a different combination of free parameters that did predict multiple images. No counter images brighter than magnitude 27 were found in the area where counterpart images were predicted.

The two complementary lensing models we adopted predicted a highly elongated image. Although the observed source is elongated along the direction predicted by the lensing models, the level of elongation was lower than the model predictions. As a result, the intrinsic image in the source plane was not circular. However, as the magnification especially close to the critical curves is one of the more sensitive quantities to measure, this probably resulted from statistical and potential systematic uncertainties in the lens modeling. We anticipate future improvements in modeling to reduce such potential systematic errors.

6. Image deconvolution

The drizzled F160W-band image was deconvolved using 20 iterations of Lucy-Richardson deconvolution[41,42]. The PSF was provided by a bright field star within the stacked image displaced $39''$ from the object. This was a modest amount of deconvolution, but sufficient to remove the blurring due to the PSF wings, and to provide a model-independent representation of the object.

After deconvolution, the extent of the source was significant out to $\approx\ 0''.3$ from its center. The distribution of light for $0''.13 \leq r \leq 0''.33$ is roughly exponential with a scale length of $0''.067 \pm 0''.005$. The isophote ellipticity over the fitted region increases with radius to ~ 0.5 at $r = 0''.33$. The half-light radius of the source is $r < 0''.13$, or 0.55 kpc (kiloparsec).

Using the detailed lens model for MACS J1149.6+2223 and the PSF-deconvolved F160W image, we reconstructed the MACS1149-JD image in the source plane at $z = 9.6$. The source-plane reconstruction is shown in Figure S3. The candidate is significantly elongated in the source plane along a position angle of 139 degrees and is well-fit by a 2D Gaussian. The Gaussian fit shows that the candidate has an axis ratio of 7.55. Assuming 4.28 kpc arcsec^{-1} at $z = 9.6$, the source spans 1.28 kpc and 0.17 kpc along its major and minor axis, respectively. Note that the most significant elongation is in the F140W band.

If MACS1149-JD is at $z = 9.6$ then its intrinsic (delensed) size is 0.14 kpc. The expected delensed size of galaxies at this redshift from extrapolations at lower ($z \sim 2{-}8$) redshifts[43] predicts objects with sizes of $r = 0.36^{+0.89}_{-0.26}$ kpc. These two values are consistent at the 0.85σ level. If our object was really at $z \sim 3$, its delensed size would be 0.41 kpc. The corresponding value from existing (unlensed) field surveys is $1.3^{+1.4}_{-0.7}$ kpc for the $z \sim 3$ galaxy population, yielding a difference with the MACS1149-JD size at the 1.3σ level. The high-redshift solution thus yields marginally better agreement with the existing observational constraints.

7. Spectral energy distribution modeling

Our SED modeling constructed a large suite of models using Monte Carlo draws of the free parameters, and then evaluated the posterior probability distribution of each parameter by calculating the statistical likelihood of each model. To fit MACS1149-JD we synthesized photometry in the 19 observed bands for $50,000$ models assuming a fixed redshift of $z = 9.6$. We parameterized the star formation history $\psi(t)$ as a delayed τ model, $\psi(t) \propto t\exp(-t/\tau)$, where t is the time since the onset of star formation and τ is a characteristic time scale. The advantage of this parameterization is that it allows for both linearly rising ($t/\tau \ll 1$) and exponentially declining ($t/\tau \gg 1$) star formation histories. We drew τ from a uniform distribution of between 10 Myr and 1 Gyr, t uniformly from $5 - 500$ Myr, and the stellar metallicity in the range $Z = 0.0002 - 0.02$ ($1\% - 100\%$ solar). For our fiducial modeling we assumed no dust obscuration, although we tested the effect of relaxing this assumption below.

Figure S4 shows the posterior probability distributions on the stellar mass, SFR, and SFR-weighted age, $\langle t\rangle_{\mathrm{SFR}} \equiv \int_0^t \psi(t')(t-t')\,\mathrm{d}t' / \int_0^t \psi(t')\,\mathrm{d}t'$. Since we were unable to place any significant constraints on either τ or the metallicity Z, we do not show these probability distributions here. Based on the median of the posterior probability distributions, our Bayesian analysis suggested a stellar mass of $\sim 1.5 \times 10^8$ $(\mu/15)^{-1}$ $M_\odot$ for MACS1149-JD, and a SFR of ~ 1.2 $(\mu/15)^{-1}$ $M_\odot$ year^{-1}. Although the probability distribution on $\langle t \rangle_{\rm SFR}$ is not peaked, we found that 95% of the models have $\langle t \rangle_{\rm SFR} < 200$ Myr, suggesting a likely formation redshift $z_f < 14.2$. This analysis clearly demonstrated the need for precise IRAC photometry of high-redshift galaxies, in order to place their physical properties on firmer quantitative footing.

We investigated the effect of changing our prior assumptions on these results. First, we considered an ensemble of models that include dust, allowing the rest-frame V-band attenuation[44] to range from $0-2$ magnitudes. This analysis yielded median stellar mass and SFR estimates that were a factor of ~ 6 higher, but with no improvement in the likelihood, and no constraint on the V-band attenuation. However, our constraints on z_f changed by $< 5\%$. We also considered simple exponentially declining star formation histories; those yielded similar estimates for the stellar mass and SFR (within a factor of ~ 2) with respect to our fiducial model parameters, and constrained the formation redshift to $z_f < 17.5$.

Nebular emission can have a significant effect[45] on the broad-band photometry of galaxies, and therefore we examined its potential effect on our SED modeling. The possibility for a contribution from either Hβ 486.1 nm or [O III] 495.9,500.7 nm was excluded because the non-detection in the F105W band firmly places the source at redshift $z > 9$, and the observed Hβ and [O III] wavelengths are beyond the spectral range of IRAC channel 2. The only relevant emission line, therefore, is [O II] 372.7 nm, which is redshifted to $3.87 - 4.02$ μm, right in the gap between IRAC channels 1 and 2 between redshift $z = 9.4 - 9.8$. Momentarily neglecting the potential effect of [O II] on our photometry, we converted the inferred posterior distribution of SFR based on our fiducial SED-modeling assumptions (Figure S4) to a posterior distribution on [O II] equivalent width[46]. Based on this distribution, we conservatively estimated a maximum equivalent width of 10 nm in the rest frame for MACS1149-JD, which would boost the IRAC channel-2 magnitude by at most 0.2 magnitude. However, we verified that removing the potential effect of this nebular emission from our IRAC photometry and refitting has a negligible effect on our estimates of stellar mass, SFR, and age.

We also tested the possibility that MACS1149-JD is an intermediate-redshift interloper (see Figure S5), with `iSEDfit`, even though the task and its library are not optimized for redshift estimations. Assuming a representative value of $z = 3.2$ (Figure 3 and S5), we constructed a suite of $50,000$ models with exponentially declining star formation histories spanning a wide range of stellar metallicity ($0.0002 - 0.03$), dust attenuation ($A_V = 0 - 3$ magnitude), age (5 Myr to 2 Gyr , where 2 Gyr is the age of the Universe at this redshift), and τ ($0.01 - 10$ Gyr). Assuming an intermediate-redshift solution, the best-fit model had a reduced $\chi^2 = 4.1$ (d.o.f = 18), compared to $\chi^2 = 1.4$ when assuming a redshift $z = 9.6$. In addition, as shown in the inset to Figure S5, the χ^2 distributions of the full suite of models assuming $z = 9.6$ peaked around $\chi^2 \approx 1.5$ (light blue histogram), whereas the χ^2 distribution of the bulk of the models assuming $z = 3.2$ are centered around $\chi^2 \approx 9$ (gray histogram). This analysis demonstrated that the high-redshift solution is preferred from the point-of-view of the SED modeling, consistent with LPZ and BPZ.

The magnification from gravitational lensing allows us to estimate the age and mass of galaxies otherwise too faint to study. Figure S6 plots the *HST* and IRAC magnitudes for a number of objects[30] at $z \sim 7 - 8$. Our measurements follow a similar between the rest-frame ultra-violet (UV) and optical magnitudes, but with considerably higher accuracy at the source's intrinsic magnitude, thanks to the gravitational magnification.

We also studied the mass-luminosity relation for MACS1149-JD. Based on an absolute magnitude of -21.8 at 150 nm in the rest frame and a magnification factor $\mu = 15$, we calculated the intrinsic magnitude $M_{150nm} = -18.8$. With a stellar mass of $\sim 1.5 \times 10^8$ $M_\odot$, this is within 10% from the value extrapolated from the mass-luminosity relation at $z \sim 4$.[47]

8. Density of star-forming rate at $z\sim$10

MACS1149-JD provides insights into the $z \sim 10$ Universe, and it is interesting to compare the object's properties with its counterparts at redshifts $z \sim 7-8$.[48,49] The search that revealed MACS1149-JD involved 12 CLASH clusters and reached a limiting magnitude of 26.3. Candidates as faint as $M_{150nm} = -18.3$ should therefore have been found in the area where the magnification factor is lower than our fiducial value, namely down to $\mu = 9$. Based on the lens models built for these clusters[8,50,51], we calculated the total volume probed above this threshold magnification. For a redshift shell between $z = 9-10$, and accounting for lens modeling uncertainty, coverage uncertainty due to areas obscured by foreground galaxies and cosmic variance[52], we calculated the effective volume to be 1220^{+366}_{-610} Mpc^3. Based on this, and the Poisson uncertainty from the discovery of a single object with an estimated star formation rate of ~ 1.2 M$_\odot$ year^{-1} assuming a Chabrier IMF, the implied star formation rate density is $(1.0^{+2.4}_{-0.6}) \times 10^{-3}$ M$_\odot$ Mpc^{-3}year^{-1}. To compare with the HUDF result based on the Salpeter IMF[54], we scaled up the value by a factor of 1.8, *i.e.*, to $(1.8^{+4.3}_{-1.1}) \times 10^{-3}$ M$_\odot$ Mpc^{-3}year^{-1}. This value is higher than the limit derived from the HUDF[9,53], but lower than an extrapolation from lower redshifts and with the amount of star formation rate density expected from the census of assembled stellar mass prior to that epoch. However, the SFR density based on a single object is highly uncertain.

9. Solar system and galactic interlopers

We verified that MACS1149-JD is not a solar system object by placing an upper limit on its proper motion over the course of 80 days. The object is also inconsistent with being a late-type Galactic star – there are no L,M,T, or Y dwarfs whose total flux difference is within 6.8σ of the observed colors of MACS1149-JD. The likelihood that the source is at an intermediate redshift is extremely low given the *Spitzer*/IRAC photometric constraints. We also studied several pairs of flux ratios in different bands for all the objects in our CLASH database with similar magnitudes. The hypothesis that the source's extremely red color is just due to photometric scatter of the general faint extragalactic population is excluded at 99.985% confidence level.

We demonstrate here that the likelihood that MACS1149-JD is either a faint solar system or Galactic object is extremely low. CLASH observations of MACS J1149.6+2223 were obtained at eight different epochs and our F140W and F160W images, in particular, cover five of those epochs spanning 80 days between December 20, 2010 and March 10, 2011. At each epoch, we measured the relative separation between MACS1149-JD and a bright early type galaxy with a compact core that is $\sim 10''$ away. This galaxy provided our common stationary astrometric reference point. The relative offsets, as a function of time, with respect to the mean separation between MACS1149-JD and the reference galaxy are shown in Figure S7. Based on these measurements, the proper motion of the source is $< 0''.13$ per year. If MACS1149-JD were an object on a low-eccentricity orbit within the solar system, its orbital period would have to be in excess of 10 million years - implying an orbital semi-major axis that is at least two orders of magnitude beyond the distance of Kuiper belt and Trans-Neptunian objects ($40 - 100$ astronomical units[AU]). Only objects in the Oort cloud ($\sim 50,000$ AU) would be expected to have such small proper motions but both the predicted absolute magnitudes and colors of typical Oort cloud objects[55] would be inconsistent with those of MACS1149-JD (MACS1149-JD is about 9 magnitudes brighter than what is expected for a 20 km wide Oort cloud object).

To assess whether MACS1149-JD could be a cool Galactic star, we compared its colors to a sample of 75 stellar templates of L,M,T dwarfs compiled from a spectral atlas[56,57] and Y dwarfs from stellar model atmospheres[58]. For each star we computed its predicted flux in F814W, F105W, F110W, F125W, F140W, F160W, IRAC 3.6 μm and 4.5 μm bands and normalized the fluxes so they match the F160W measurement for MACS1149-JD. We then computed, for each star, the corresponding total flux deviation from the MACS1149-JD flux values using the expression:

$$\langle \Delta f \rangle = \sqrt{\Sigma_{i=1}^{N} \left[(f_{i,MACS1149-JD} - f_{i,STAR})/\sigma_{i,obj} \right]^2} \quad (1)$$

where the sum is over the eight bands. There were no L,M,T, or Y dwarfs whose total flux difference is within 6σ of the observed colors of MACS1149-JD(see also Figure S8). Indeed, the minimum difference in flux space between the source and the closest stellar match is 6.8σ and the median difference is 16.8σ. The combination of near-infrared detections and upper limits measured for MACS1149-JD thus argues strongly against a cool, faint Galactic star as the likely explanation for the source.

10. Photometric scatter test

We demonstrate that the photometry of MACS1149-JD is not likely to be due to drawing randomly from the main faint galaxy population. We extracted from all 12 CLASH cluster object catalogs derived from IR-based detection images those sources that have approximately similar WFC3 F160W fluxes as MACS1149-JD. The selection criterion is magnitude $25.45 < \mathrm{F160W} \leq 26.95$. There were a total of 5614 objects that satisfy this criterion. We then generated new magnitudes for each object by randomly drawing, from a Gaussian distribution, with a mean equal to the object's measured flux and with a standard deviation equal to the object's flux uncertainty. We then counted how many such objects would have measured flux ratios that lie within the 1σ uncertainty of the F110W/F125W and F125W/F160W flux ratios of MACS1149-JD and that also show no flux (at the 2σ level) in the F814W and F105W bands. We ran 1000 such realizations of the sample and found that only 0.015% of the objects (averaged over 1000 realizations) would satisfy these criteria. Thus, MACS1149-JD is unique amongst the population of faint sources at the 99.985% level (Figure S9).

11. Summary

We carried out extensive analyses to study the nature of such an object with unique properties and found the following evidence:

- Detection of the source at multiple epochs in both *HST* and *Spitzer* imaging rules out the source being a spurious detection or a transient object.
- The combination of color decrements at ~ 1.3 μm and ~ 4 μm favor a high-redshift solution
- Intermediate-redshift fits yield significantly higher values of χ^2 using just *HST* photometry alone.
- Intermediate-redshift solutions are ruled out at 4σ when *HST* and *Spitzer* photometry are used in photometric redshift estimation.
- The de-lensed magnitude is consistent with expectations for sources at $z > 8$.
- The de-lensed half-light radius is more consistent with expectations for sources at $z > 8$.
- The source plane morphology is significantly more elongated than the image plane morphology.
- The proper motion upper limit and the source's apparent magnitude make it very unlikely that the source is a Kuiper Belt, Trans Neptunian or Oort cloud object.
- Location of the source in multi-color space is inconsistent (at 4σ) with the source being a cool Galactic dwarf star (spectral type L,M,T,Y).
- Photometric scatter is not sufficient to explain colors, and this explanation is rejected at the 99.985% confidence level.

We therefore conclude that the MACS1149-JD is highly unlikely to be an intermediate-redshift interloper, a cool, late-type star, or solar system object. The most probable explanation is a $z = 9.6$ galaxy.

31. Blakeslee, J. P., Anderson, K. R., Meurer, G. R., Benítez, N., & Magee, D. An automatic image reduction pipeline for the advanced camera for surveys, in *Astronomical Data Analysis Software and Systems XII* (San Francisco: ASP), eds. H. E. Payne, R. I. Jedrzejewski, & R. N. Hook, **295**, 257-260 (2003).

32. Koekemoer, A. M., Frutcher, A. S., Hook, R. N., & Hack, W. MultiDrizzle: an integrated pyraf script for registering, cleaning and combining images, in *The 2002 HST Calibration Workshop: Hubble after the Installation of the ACS and the NICMOS Cooling System*, ed. S. Arribas, A. Koekemoer, & B. Whitmore, 337-340 (2003).

33. Koekemoer, A. M., et al. CANDELS: the cosmic assembly near-infrared deep extragalactic legacy survey - the Hubble space telescope observations, imaging data products, and mosaics, *Astrophys. J. Suppl.*, **197**, 36 (2011).

34. Bertin, E., & Arnouts, S. SExtractor: software for source extraction, *A&Ap Suppl.*, **117**, 393-404 (1996).

35. Peng, C. Y., Ho, L. C., Impey, C. D., & Rix, H.-W. Detailed structural decomposition of galaxy images, *Astron. J.*, **124**, 266-293 (2002).

36. Eyles, L. P., et al. Spitzer imaging of i'-drop galaxies: old stars at $z \sim 6$, *Mon. Not. R. Astron. Soc.*, **364**, 443-454 (2005).

37. Dunkley, J., Bucher, M., Ferreira, P. G., Moodley, K., & Skordis, C. Fast and reliable Markov chain Monte Carlo technique for cosmological parameter estimation *Mon. Not. R. Astron. Soc.*, **356**, 925-936 (2005).

38. Kneib, J.-P., Mellier, Y., Fort, B., & Mathez, G. The Distribution of dark matter in distant cluster lenses: modelling A370, *A&Ap*, **273**, 367-376 (1993).

39. Navarro, J. F., Frenk, C. S., & White, S. D. M. The Structure of cold dark matter halos, *Astrophys. J.*, **463**, 563-575 (1996).

40. Limousin, M., Kneib, J.-P., & Natarajan, P. Constraining the mass distribution of galaxies using galaxy-galaxy lensing in clusters and in the field, *Mon. Not. R. Astron. Soc.*, **356**, 309-322 (2005).

41. Lucy, L. B. An interactive technique for the rectification of observed distributions, *Astron. J.*, **79**, 745-753 (1974).

42. Richardson, W. H. Bayesian-based iterative method of image restoration, *J. Opt. Soc. A.*, **62**, 55-59 (1972).

43. Oesch, P. A., et al. Structure and morphologies of $z \sim 7-8$ galaxies from ultra-deep WFC3/IR imaging of the Hubble ultra-deep field, *Astrophys. J.*, **709**, L21-25 (2010).

44. Calzetti, D., et al. The dust content and opacity of actively star-forming galaxies, *Astrophys. J.*, **533**, 682-695 (2000).

45. Shim, H., et al. $z \sim 4$ Hα emitters in the great observatories origins deep survey: tracing the dominant mode for growth of galaxies, *Astrophys. J.*, **738**, 69 (2011).

46. Kennicutt, R. C., Jr., Star Formation in Galaxies Along the Hubble Sequence, ARA&A, **36**, 189-232 (1998).

47. González, V., et al. Evolution of galaxy stellar mass functions, mass densities, and mass-to-light ratios from $z \sim 7$ to $z \sim 4$, *Astrophys. J.*, **735**, L34 (2011).

48. Bradley, L. D., et al. The Brightest of reionizing galaxies survey: constraints on the bright end of the $z \sim 8$ luminosity function, *Astrophys. J.*, submitted, arXiv 1204.3641 (2012).

49. Dunlop, J. S. Observing the first galaxies, arXiv 1205.1543 (2012)

50. Zitrin, A., et al. The cluster lensing and supernova survey with Hubble (CLASH): strong-lensing analysis of A383 from 16-band HST/WFC3/ACS imaging, *Astrophys. J.*, **742**, 117 (2011).

51. Zitrin, A., et al. CLASH: new multiple images constraining the inner mass profile of MACS J1206.2-0847, *Astrophys. J.*, **749**, 97 (2012).

52. Trenti, M. & Stiavelli, M. Cosmic Variance and Its Eect on the Luminosity Function Determination in Deep High-z Surveys, *Astrophys. J.*, **676**, 767-780 (2008).

53. Bouwens, R. J., et al. Ultraviolet luminosity functions from 132 $z \sim 7$ and $z \sim 8$ Lyman-break galaxies in the ultra-deep HUDF09 and wide-area early release science WFC3/IR observations, *Astrophys. J.*, **737**, 90 (2011).

54. Salpeter, E. E. The luminosity function and stellar evolution *Astrophys. J.*, **121**, 161-167 (1955).

55. Sheppard, S. S. The colors of extreme outer solar system objects, *Astron. J.*, **139**, 1394-1405 (2010).

56. Rayner, J. T., Cushing, M. C. & Vacca, W. D. The infrared telescope facility (IRTF) spectral library: cool stars, *Astrophys. J. Suppl.*, **185**, 289-432 (2009).

57. Cushing, M. C., Rayner, J. T. & Vacca, W. D. An infrared spectroscopic sequence of M, L, and T dwarfs, *Astrophys. J.*, **623**, 1115-1140 (2005).

58. Hubeny, I., & Burrows, A. A systematic study of departures from chemical equilibrium in the atmospheres of substellar mass objects, *Astrophys. J.*, **669**, 1248-1261 (2007).

Table S1: Photometry of MACS1149-JD

Band	Coverage (μm)	Magnitude	Flux (nJy)
IRAC 2	4.0-5.0	24.8 ± 0.3	449 ± 138
IRAC 1	3.2-3.9	$> 26.1^a$	86 ± 138
F160W	1.40-1.67	25.70 ± 0.07	194 ± 12
F140W	1.20-1.58	25.92 ± 0.08	156 ± 12
F125W	1.10-1.39	26.8 ± 0.2	70 ± 14
F110W	0.93-1.37	27.5 ± 0.3	36 ± 10
F105W	0.92-1.19	$> 28.7^a$	5 ± 12
F850LP	0.88-1.00	$> 28.1^a$	-66 ± 21
F814W	0.71-0.96	$> 29.1^a$	-2 ± 8
F775W	0.70-0.85	$> 28.2^a$	6 ± 18
F625W	0.56-0.70	$> 28.5^a$	-25 ± 15
F606W	0.47-0.71	$> 28.9^a$	2 ± 10
F555W	0.47-0.60	$> 28.9^a$	3 ± 10
F475W	0.40-0.55	$> 28.7^a$	-24 ± 12
F435W	0.38-0.48	$> 28.5^a$	10 ± 14
F390W	0.35-0.44	$> 28.5^a$	-11 ± 14
F336W	0.31-0.36	$> 26.6^a$	46 ± 80
F275W	0.25-0.29	$> 27.6^a$	18 ± 32
F225W	0.21-0.26	$> 26.4^a$	-26 ± 99

[a] 1σ detection limit. For negative fluxes, we conservatively assume zero flux when calculating the 1σ upper limit.

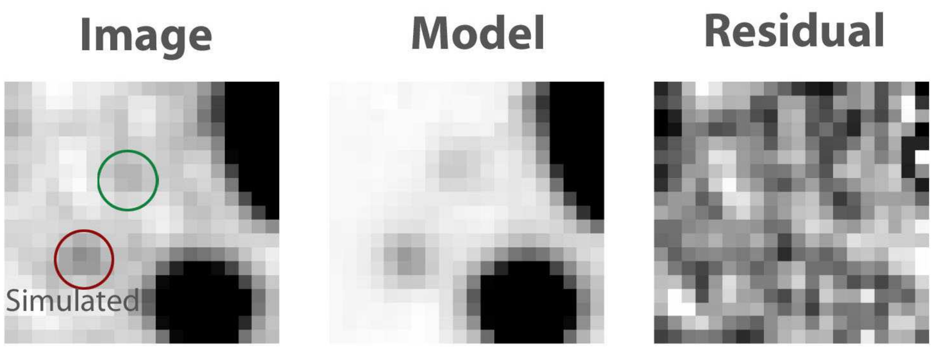

Figure S1 – Illustration of IRAC fitting at 4.5μm. In the left panel, MACS1149-JD is marked with a green circle, and a simulated point source of AB=24.0 is marked with a red circle. In the middle panel, the best-fit `GALFIT` model is displayed, and in the right panel, the residual image with all model components subtracted. Note that the actual fitting is made without simulated sources and yields a mean magnitude of 24.8$\pm$0.3.

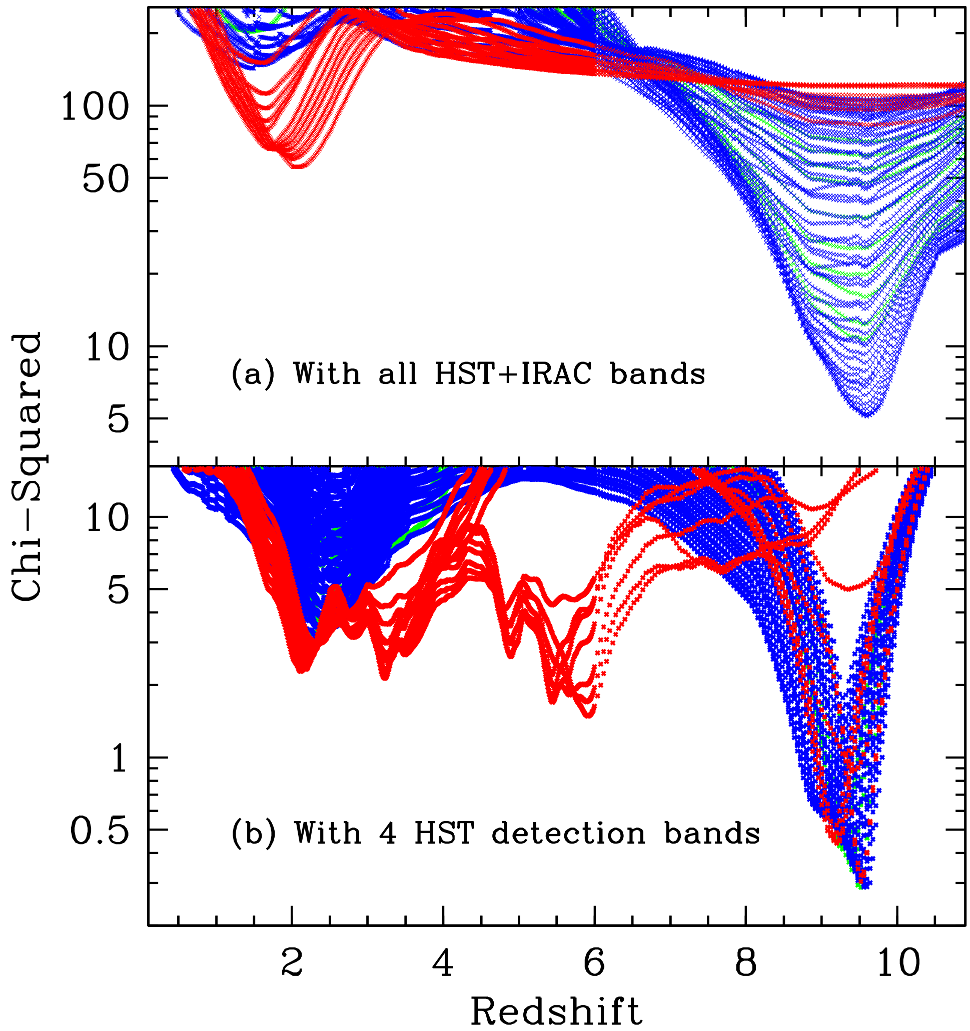

Figure S2 – Likelihood distribution of photometric redshift. The χ^2 values are plotted at different fitted redshifts for each template in the LPZ template library, plus the effect of dust attenuation. Red points: early types; green points: intermediate type; and blue points: late type. In panel (a), we fit all the data in 17 *HST* bands and two IRAC bands (d.o.f = 16). Intermediate-redshift solutions yield considerably higher χ^2 values than the high-redshift solutions. In panel (b), we fit only the data in the four *HST* bands where the source is detected (d.o.f = 1), to show extreme, but not viable, intermediate-redshift solutions at low probability.

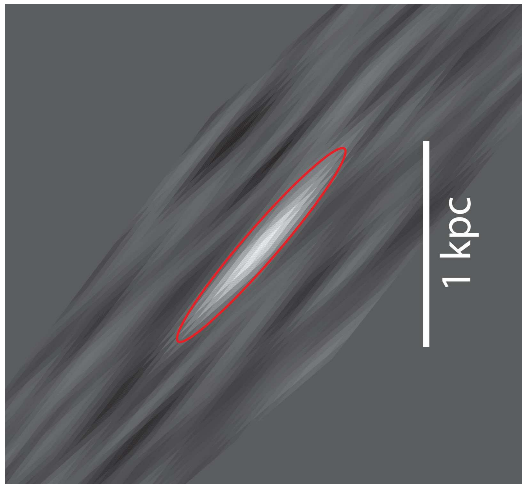

Figure S3 – Source-plane reconstruction of MACS1149-JD in the WFC3/IR F160W band. The source is significantly elongated with an axis ratio of 7.55. The candidate spans 1.28 kpc and 0.17 kpc along its major and minor axis, respectively, as denoted by the red ellipse. The results are sensitive to the model details and systematic errors.

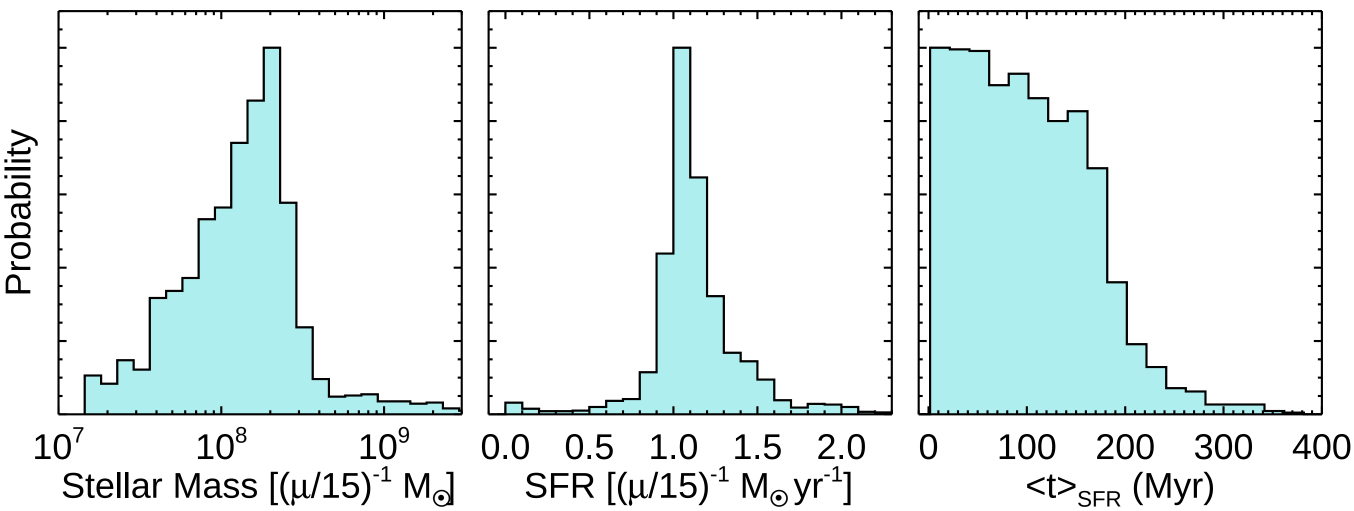

Figure S4 – Posterior probability distributions on the stellar mass, SFR, and SFR-weighted age, $\langle t\rangle_{\rm SFR}$ based on our Bayesian SED modeling. Note that our stellar mass and SFR estimates have been de-magnified assuming a fiducial magnification factor μ=15, while $\langle t\rangle_{\rm SFR}$ is independent of μ. Based on this analysis we infer a stellar mass of $\sim 1.5\times10^{8}\ (\mu/15)^{-1}$ $M_\odot$ a SFR of $\sim 1.2\ (\mu/15)^{-1}$ $M_\odot$ year^{-1}, and a constrain on the SFR-weighted age of <200 Myr (95% confidence level), implying a formation redshift z_f <14.2.

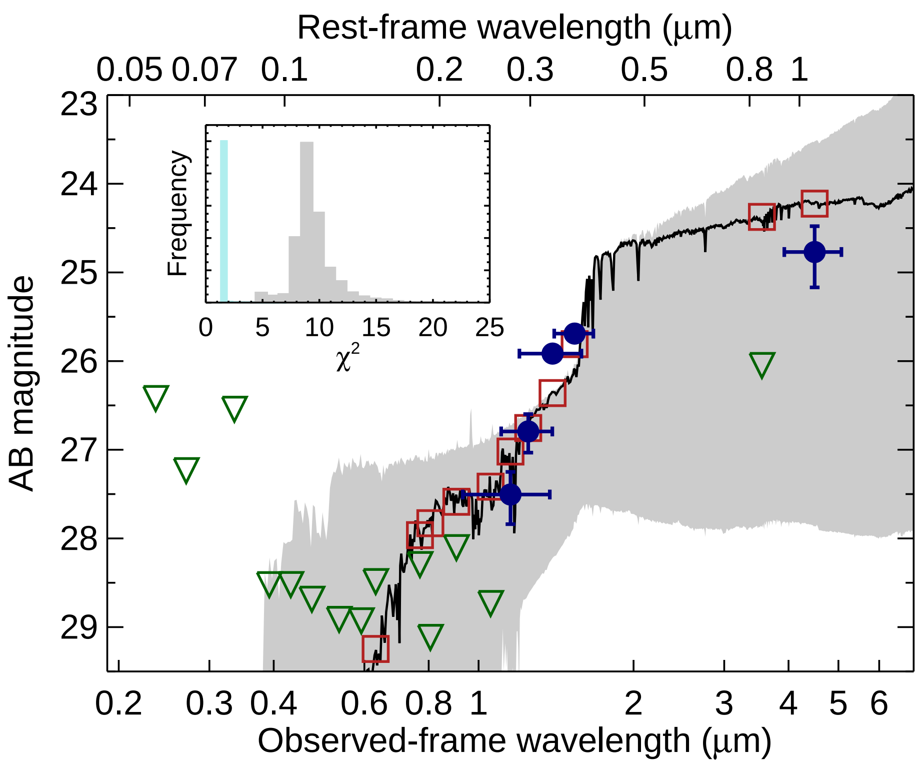

Figure S5 – Results of modeling the SED of MACS1149-JD assuming an intermediate-redshift solution, z=3.2. This figure is analogous to Fig. 4 but here the gray shading shows the range models drawn from the posterior probability distribution that fit the data assuming z=3.2. The black spectrum is the best-fit z=3.2 model, and the open red squares show the photometry of this model convolved with the WFC3, ACS, and IRAC filter response functions. As shown in the inset, the χ^2 distribution of these intermediate-redshift models peaks around χ^2 ≈9 (d.o.f. 18, gray histogram), whereas the χ^2 distribution of the models fitted to the data assuming z=9.6 peaks around χ^2 ≈1.5 (light blue histogram; see also Fig. 4). We conclude, therefore, that the high-redshift solution is clearly preferred from the point-of-view of our SED modeling.

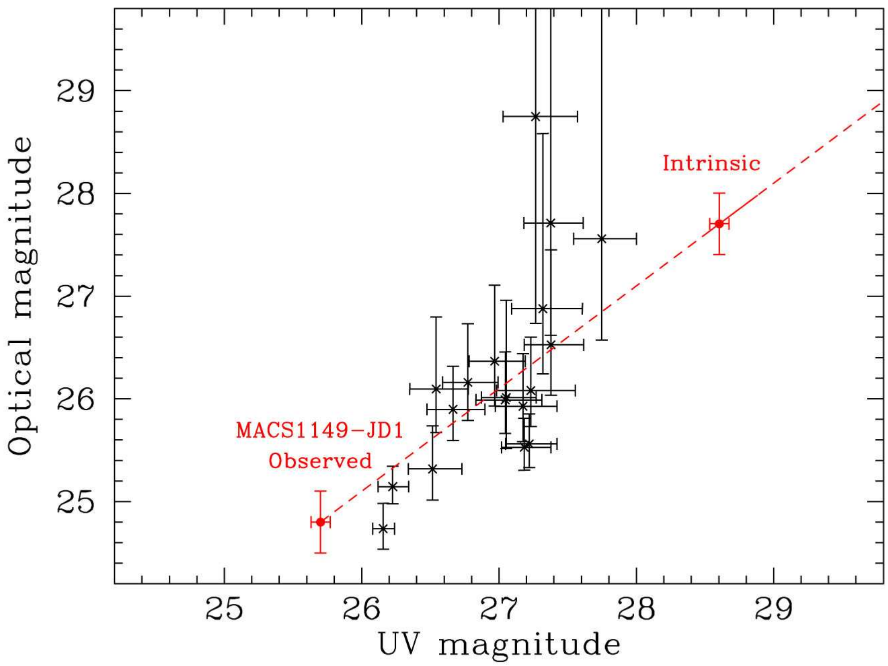

Figure S6 – UV and optical magnitudes of high-redshift objects. The data[30] are from objects at $z{\sim}7$-8. The rest-frame UV band is F125W, and the rest-frame optical band is the IRAC 3.6μm. The magnitudes of MACS1149-JD, in F160W and 4.5 μm bands, are plotted in red, in their observed values (the lower point) and de-magnified values (scaled down by a flux factor of 15, at the upper-right). The dashed red line is the track of the source's intrinsic magnitudes under different magnification factors, and the solid red line marks the range for MACS1149-JD. Cluster lensing makes it possible to improve the accuracy of photometry at the faint end.

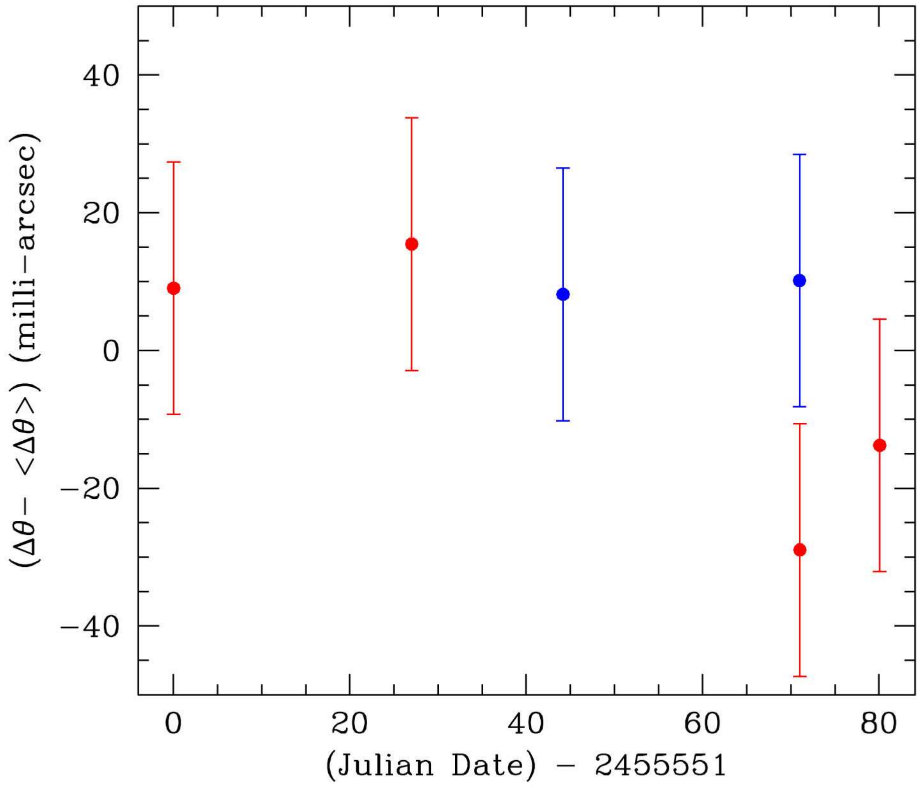

Figure S7 – Relative difference, in milli-arcseconds, between the separation of MACS1149-JD from a nearby reference galaxy at each of five separate epochs and the mean separation value. The upper limit on its proper motion is $< 0''.13$ year^{-1}.

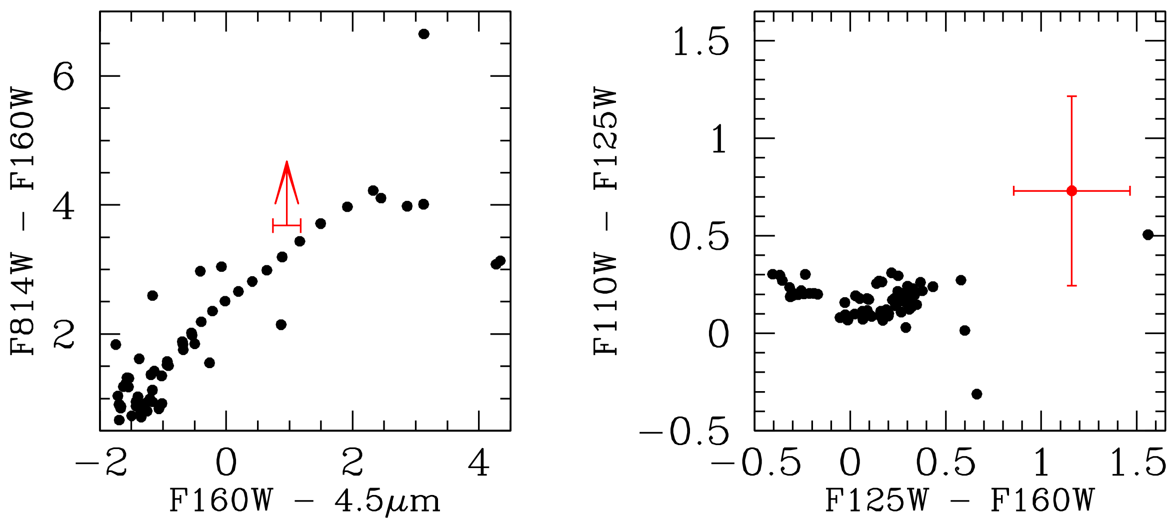

Figure S8 – Comparison of colors of 75 late-type stars[56–58] (black circles) and those of the high-redshift candidate MACS1149-JD (red circle). The F814W magnitude for MACS1149-JD is based on its 1σ upper limit. In the right panel, the color of a rare M-8III star is close to the error box, but it is well separated in color in the left panel. If we run the analysis using 2σ error, the median separation drops from 16.8σ to 11.2σ, and the minimum separation drops from 6.8σ to 4.6σ. The candidate object is still well isolated from the main population.

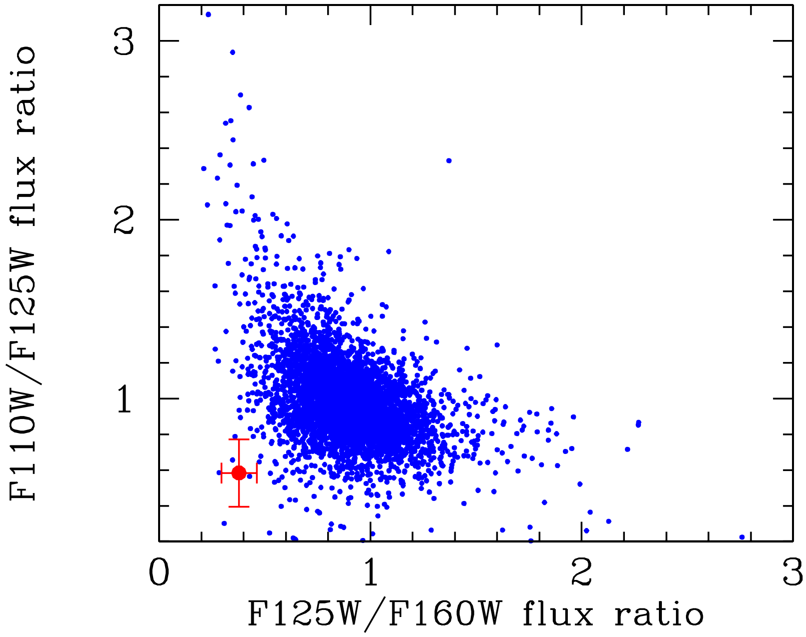

Figure S9 – Flux ratios of faint galaxy population in the CLASH database with F160W magnitude 25.45−26.85. MACS1149-JD, a resolved source is marked by a red circle. The plotted fluxes are isophotal values and hence are slightly different from Table S11. The five sources next to or within the error box are further examined, and they are rejected because of a detection in optical bands.